

# The Interplay of the Solar Wind Core and Suprathermal Electrons: A Quasilinear Approach for Firehose Instability

S.M.SHAABAN,<sup>1,2</sup> M. LAZAR,<sup>1,3</sup> P.H.YOON,<sup>4,5,6</sup> AND S. POEDTS<sup>1</sup>

<sup>1</sup>*Centre for Mathematical Plasma Astrophysics, KU Leuven, Celestijnenlaan 200B, B-3001 Leuven, Belgium*

<sup>2</sup>*Theoretical Physics Research Group, Physics Dept., Faculty of Science, Mansoura University, 35516, Mansoura, Egypt*

<sup>3</sup>*Institut für Theoretische Physik, Lehrstuhl IV: Weltraum- und Astrophysik, Ruhr-Universität Bochum, D-44780 Bochum, Germany*

<sup>4</sup>*Institute for Physical Science and Technology, University of Maryland, College Park, MD 20742, USA*

<sup>5</sup>*Korea Astronomy and Space Science Institute, Daejeon 34055, Korea*

<sup>6</sup>*School of Space Research, Kyung Hee University, Yongin, Gyeonggi 17104, Korea*

(Received February 1, 2019; Revised , 2018; Accepted , 2018)

Submitted to ApJ

## ABSTRACT

In the solar wind an equipartition of kinetic energy densities can be easily established between thermal and suprathermal electrons and the instability conditions are markedly altered by the interplay of these two populations. The new thresholds derived here for the periodic branch of firehose instability shape the limits of temperature anisotropy reported by the observations for both electron populations. This instability constraint is particularly important for the suprathermal electrons which, by comparison to thermal populations, are even less controlled by the particle-particle collisions. An extended quasilinear approach of this instability confirms predictions from linear theory and unveil the mutual effects of thermal and suprathermal electrons in the relaxation of their temperature anisotropies and the saturation of growing fluctuations.

*Keywords:* solar wind — plasmas — instabilities — waves

## 1. INTRODUCTION

In collision-poor plasmas in space, e.g., the solar wind and planetary environments, the decay of free energy from large scales is mediated by the instabilities and the observed enhanced fluctuations (Štverák et al. 2008; Gary et al. 2016; Gershman et al. 2017). For instance, the beam-plasma instabilities should play a major role in the dissipation of solar plasma outflows, e.g., from coronal holes or during coronal mass ejections (CMEs) (Ganse et al. 2012; Jian et al. 2014), while an increase of temperature anisotropy  $T_{\parallel} > T_{\perp}$  (where  $\parallel, \perp$  refer to directions relative to the interplanetary magnetic field), as predicted by the CGL invariants (Chew et al. 1956) at large heliocentric distances (where particle-particle collisions are inefficient), is expected to be constrained by the firehose instability (Štverák et al. 2008; Lazar et al. 2017b). In a quiet solar wind, e.g., during slow winds, the observations seem to confirm a potential role of this instability, and that is, surprisingly, for the quasi-thermal (bi-Maxwellian) populations whose large deviations from isotropy appear to be well shaped by the instability thresholds predicted by the kinetic the-

ory (Kasper et al. 2006; Hellinger et al. 2006; Štverák et al. 2008). However, an important amount of kinetic (free) energy is transported by the suprathermal particle populations, which are ubiquitous in space plasmas and are well described by the Kappa power-laws (Vasyliunas 1968; Pierrard & Lazar 2010). We need therefore to take into account the effects of these populations for a realistic description of firehose instability in the solar wind context.

Recent attempts to characterize these effects are either limited to a linear analysis (Lazar & Poedts 2009; Lazar et al. 2015, 2017a; Vinās et al. 2017), or simply altered by an idealized (bi-)Maxwellian description of suprathermal populations in a quasilinear analysis. Thus, quasilinear approaches have been successfully proposed for both the whistler and firehose instabilities driven either by a single bi-Maxwellian population of electrons (Yoon et al. 2012, 2017a; Sarfraz et al. 2017), or by dual electrons with a core-halo structure (Sarfraz et al. 2016; Sarfraz 2018) minimizing, however, the effects of suprathermals by assuming the halo bi-Maxwellian distributed. Here we present a quasilinear approach of firehose instability driven by the anisotropic

electrons, i.e.,  $A \equiv T_{\parallel}/T_{\perp} < 1$ , adopting an advanced dual model for the electron velocity distributions, as indicated by the observations in the solar wind (Štverák et al. 2008; Maksimovic et al. 2005; Pierrard et al. 2016). This model combines two main components, a thermal bi-Maxwellian core at low energies, and a suprathermal bi-Kappa halo which enhances the high-energy tails of the distributions. An additional strahl can be detected (mainly during fast winds) streaming anti-sunwards along the magnetic field, but at large enough distances from the Sun, e.g., beyond 1 AU, the strahl diminishes considerably (probably scattered by the self-generated instabilities) and a dual core-halo composition remains fairly dominant (Maksimovic et al. 2005).

The instability develops from the interplay between the core (subscript  $c$ ) and halo (subscript  $h$ ) electrons, and the highest growing modes (with the lowest thresholds) are therefore expected to arise from a cumulative effect when both populations exhibit similar anisotropies  $A_{c,h} < 1$ . We assume a homogenous plasma dominated by the electrons and protons, and neglect the effects of any other minor species that can be present in the solar wind. In section 2 we first introduce the velocity distribution functions, a dual core-halo model for the electrons while heavier protons are assumed Maxwellian and isotropic, and then build the linear and quasilinear formalisms used to describe the dispersion and stability of firehose solutions. Derived numerically these solutions are discussed for several representative cases in section 3. We restrict to firehose modes propagating parallel to the magnetic field, especially because of the complexity of a quasilinear theory which becomes less feasible for an arbitrary propagation. By contrast to previous studies, here we adopt a new normalization for the wave parameters in order to avoid any artificial coupling between the core and halo electrons, which may alter the quasilinear relaxation under the influence of increasing firehose fluctuations. In section 4 we summarize the results and provide the main conclusions of this study.

## 2. MODELING BASED ON OBSERVATIONS

The velocity distribution functions (VDFs) of plasma particles and, in general, parametrization used for our magnetized plasma approach are characteristic to the solar wind at different heliocentric distances, but may also be relevant for more particular environments like planetary magnetospheres.

### 2.1. Solar wind electrons

The in-situ measurements collected from different missions, e.g., Ulysses, Helios 1, and Cluster II, unveil electron distributions in the slow winds ( $V_{SW} \leq 500$  km

$s^{-1}$ ) with a dual structure combining a thermal dense core (subscript  $c$ ), and a dilute suprathermal halo (subscript  $h$ ) (Maksimovic et al. 2005; Štverák et al. 2008)

$$f_e(v_{\parallel}, v_{\perp}) = \eta_c f_c(v_{\parallel}, v_{\perp}) + \eta_h f_h(v_{\parallel}, v_{\perp}). \quad (1)$$

Here,  $\eta_h = n_h/n_0$  and  $\eta_c = 1 - \eta_h$  are relative densities of the halo and core, respectively, and  $n_0$  is the total electron number density. The core population is well fitted by a bi-Maxwellian distribution (Štverák et al. 2008)

$$f_c(v_{\parallel}, v_{\perp}) = \frac{1}{\pi^{3/2} \alpha_{\perp,c}^2 \alpha_{\parallel,c}} \exp\left(-\frac{v_{\parallel}^2}{\alpha_{\parallel,c}^2} - \frac{v_{\perp}^2}{\alpha_{\perp,c}^2}\right), \quad (2)$$

with thermal velocities  $\alpha_{\parallel,\perp,c} \equiv \alpha_{\parallel,\perp,c}(t)$  (varying in time  $t$  in our quasilinear approach) defined by the corresponding temperature components (as the second-order moments of the distribution)

$$T_{\parallel,c} = \frac{m_e}{k_B} \int d\mathbf{v} v_{\parallel}^2 f_c(v_{\parallel}, v_{\perp}) = \frac{m_e \alpha_{\parallel,c}^2}{2k_B}, \quad (3a)$$

$$T_{\perp,c} = \frac{m_e}{2k_B} \int d\mathbf{v} v_{\perp}^2 f_c(v_{\parallel}, v_{\perp}) = \frac{m_e \alpha_{\perp,c}^2}{2k_B}. \quad (3b)$$

The halo component is described by an anisotropic bi-Kappa distribution function

$$f_h(v_{\parallel}, v_{\perp}) = \frac{1}{\pi^{3/2} \alpha_{\perp,h}^2 \alpha_{\parallel,h}} \frac{\Gamma(\kappa + 1)}{\Gamma(\kappa - 1/2)} \times \left[1 + \frac{v_{\parallel}^2}{\kappa \alpha_{\parallel,h}^2} + \frac{v_{\perp}^2}{\kappa \alpha_{\perp,h}^2}\right]^{-\kappa-1}, \quad (4)$$

with parameters  $\alpha_{\parallel,\perp,h} \equiv \alpha_{\parallel,\perp,h}(t)$  (varying in time  $t$  in our quasilinear approach) defined by the components of the anisotropic temperature

$$T_{\parallel,h} = \frac{2\kappa}{2\kappa - 3} \frac{m_e}{2k_B} \alpha_{\parallel,h}^2, \quad T_{\perp,h} = \frac{2\kappa}{2\kappa - 3} \frac{m_e}{2k_B} \alpha_{\perp,h}^2. \quad (5)$$

Such a plasma system we parametrize by inspiring from the observations reported by Štverák et al. (2008), from roughly 120000 events detected in the ecliptic at different distances (0.3 – 3.95 AU) from the Sun. We chose only the slow wind data ( $V_{SW} \leq 500$  km  $s^{-1}$ ), for which the density of the strahl population is faint enough to not affect the instability conditions. These data have been used in a series of recent studies to characterize the electron core and halo populations (Pierrard et al. 2016; Lazar et al. 2017a). For slow wind conditions, the suprathermal halo tails are fitted by a Kappa with  $2.5 < \kappa < 9.5$ . Comparing to the core population,

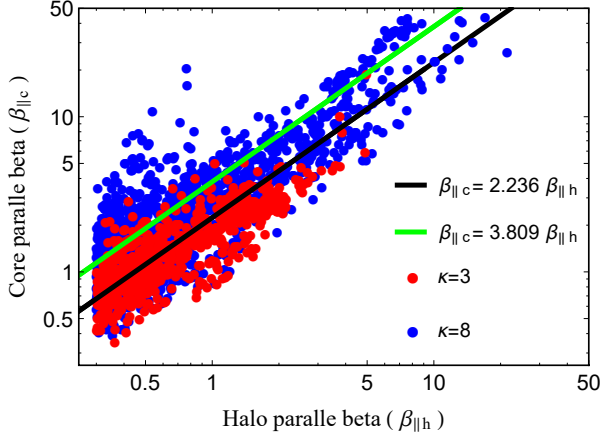


**Figure 1.** Plasma beta values measured in the solar wind for the core and halo electrons with the apparent linear correlations, for  $\kappa = 3$  (red dots and black fit) and  $\kappa = 8$  (blue dots and green fit).

the halo is hotter ( $T_h > T_c$ ) but less dense, with a number density  $\eta_h \leq 0.10$  (Maksimovic et al. 2005). Both the core and halo populations may exhibit temperature anisotropy, i.e.,  $A = T_\perp/T_\parallel \neq 1$ , which can be at the origin of kinetic instabilities, such as whistler (if  $A > 1$ ) or firehose instability (if  $A < 1$ ). Their anisotropies show a prevalent tendency for a direct (linear) correlation, like  $A_c = CA_h$ , with  $C \simeq 1$  (Pierrard et al. 2016). In the present study we are interested for the conditions most favorable to firehose instability. For the interplay of the core and suprathermal halo these conditions are those associated with similar sub-unitary anisotropies  $A_c = A_h < 1$ . We use the observations to evaluate the relative densities  $\eta_h$  and  $\eta_c$  and the ratio of parallel plasma betas  $\beta_c/\beta_h$  (where  $\beta_\parallel \equiv 8\pi n k_B T_\parallel/B^2$ ), corresponding to two different representative values of  $\kappa$ -index. Figure 1 displays a density histogram for  $\beta_c$  vs.  $\beta_h$  with a color bar counting the number of events. For a low  $\kappa = 3$  ( $2.5 \leq \kappa \leq 3.5$ ) we find relevant  $\beta_c/\beta_h \simeq 2.236$ , and for a high  $\kappa = 8$  ( $7.5 \leq \kappa \leq 8.5$ ) we consider  $\beta_c/\beta_h \simeq 3.809$ . Contrary to other recent studies which assume  $\beta_c < \beta_h$ , e.g., Sarfraz (2018, and refs. therein), here we consider  $\beta_c > \beta_h$  as suggested by the observations. A similar linear correlation between plasma beta parameters  $\beta_c$  and  $\beta_h$  is found in Lazar et al. (2015) using a different set of data from Ulysses during the slow winds. In Section 3 we show how important this ratio is for contrasting the core and halo parallel betas for the instability conditions.

## 2.2. Theory of dispersion and stability

For a collisionless and homogeneous plasma, the general, linear dispersion relation of the electromagnetic

modes propagating parallel to the background magnetic field ( $\mathbf{B}_0$ ), i.e.,  $\mathbf{k} \times \mathbf{B}_0 = 0$ ) reads

$$\frac{k^2 c^2}{\omega^2} = 1 + \sum_{a=p,c,h} \frac{\omega_{p,a}^2}{\omega^2} \int dv \frac{v_\perp}{2(\omega - kv_\parallel \pm \Omega_a)} \left( (\omega - kv_\parallel) \frac{\partial f_a}{\partial v_\perp} + kv_\perp \frac{\partial f_a}{\partial v_\parallel} \right), \quad (6)$$

where  $k$  is the wave number,  $c$  is the speed of light,  $\omega_{p,\alpha} = \sqrt{4\pi n_\alpha e^2/m_\alpha}$  and  $\Omega_a = eB_0/m_\alpha c$  are, respectively, the non-relativistic plasma frequency and the gyro-frequency of species  $a$ , and  $\pm$  denotes the right-handed (RH) and left-handed (LH) circular polarization, respectively.

For the LH electron firehose unstable modes in our plasma system the instantaneous dispersion relation (6) reduces to

$$\begin{aligned} \tilde{k}^2 = & A_p - 1 + \left( \frac{A_p \tilde{\omega} - (A_p - 1)}{\tilde{k} \sqrt{\beta_p}} \right) Z_p \left( \frac{\tilde{\omega} - 1}{\tilde{k} \sqrt{\beta_p}} \right) \\ & + \eta_c \mu \left[ A_c - 1 + \left( \frac{A_c \tilde{\omega} + (A_c - 1) \mu}{\tilde{k} \sqrt{\mu \beta_c/\eta_c}} \right) \right. \\ & \times Z_c \left( \frac{\tilde{\omega} + \mu}{\tilde{k} \sqrt{\mu \beta_c/\eta_c}} \right) \left. \right] + \eta_h \mu [A_h - 1 \\ & + \left( \frac{A_h \tilde{\omega} + (A_h - 1) \mu}{\tilde{k} \sqrt{\mu \chi_h \beta_h/\eta_h}} \right) Z_h \left( \frac{\tilde{\omega} + \mu}{\tilde{k} \sqrt{\mu \chi_h \beta_h/\eta_h}} \right) \end{aligned} \quad (7)$$

where  $\tilde{k} = kc/\omega_{p,p}$  is the normalized wave-number,  $\tilde{\omega} = \omega/\Omega_p$  is the normalized wave frequency,  $\mu = m_p/m_e$  is the proton-electron mass contrast,  $A_a = T_{\perp,a}/T_{\parallel,a} \equiv \beta_{\perp,a}/\beta_{\parallel,a}$  and  $\beta_{\parallel,\perp,a} = 8\pi n_a k_B T_{\parallel,\perp,a}/B_0^2$  are, respectively, the temperature anisotropy, and plasma beta parameters for protons (subscript " $a = p$ "), electron core (subscript " $a = c$ "), and electron halo (subscript " $a = h$ ") populations,  $\chi_h = (\kappa - 1.5)/\kappa$ ,  $\eta_h = n_h/n_0$ ,  $\eta_c = 1 - \eta_h$  are the halo and the core density contrast, respectively,

$$Z_a(\xi_a^\pm) = \frac{1}{\sqrt{\pi}} \int_{-\infty}^{\infty} \frac{\exp(-x^2)}{x - \xi_a^\pm} dx, \quad \Im(\xi_a^\pm) > 0, \quad (8)$$

is the plasma dispersion function (Fried & Conte 1961) and

$$\begin{aligned} Z_h(\xi_h^+) = & \frac{1}{\pi^{1/2} \kappa^{1/2}} \frac{\Gamma(\kappa)}{\Gamma(\kappa - 1/2)} \\ & \int_{-\infty}^{\infty} \frac{(1 + x^2/\kappa)^{-\kappa}}{x - \xi_h^+} dx, \quad \Im(\xi_h^\pm) > 0. \end{aligned} \quad (9)$$

is the generalized (Kappa) dispersion function (Lazar et al. 2008).

The time evolution of the velocity distributions are described by the particle kinetic equation in the diffusion approximation

$$\frac{\partial f_a}{\partial t} = \frac{ie^2}{4m_a^2 c^2 v_\perp} \int_{-\infty}^{\infty} \frac{dk}{k} \left[ (\omega^* - kv_\parallel) \frac{\partial}{\partial v_\perp} + kv_\perp \frac{\partial}{\partial v_\parallel} \right] \times \frac{v_\perp \delta B^2(k, \omega)}{\omega - kv_\parallel - \Omega_a} \left[ (\omega - kv_\parallel) \frac{\partial f_a}{\partial v_\perp} + kv_\perp \frac{\partial f_a}{\partial v_\parallel} \right], \quad (10)$$

where the energy density of the fluctuations  $\delta B^2(k)$  is described by the wave equation

$$\frac{\partial \delta B^2(k)}{\partial t} = 2\gamma_k \delta B^2(k), \quad (11)$$

with growth rate  $\gamma_k$  of the EFH instability. Eq. (10) is used to derive perpendicular and parallel velocity moments for protons, and electron core and halo populations, as follows

$$\frac{dT_{\perp p}}{dt} = -\frac{e^2}{2m_p c^2} \int_{-\infty}^{\infty} \frac{dk}{k^2} \langle \delta B^2(k) \rangle \times \left\{ (2A_p - 1) \gamma_k + \text{Im} \frac{2i\gamma - \Omega_p}{k\alpha_{\parallel p}} F^-(A_p, \Omega_p, Z_p) \right\} \quad (12a)$$

$$\frac{dT_{\parallel p}}{dt} = \frac{e^2}{m_p c^2} \int_{-\infty}^{\infty} \frac{dk}{k^2} \langle \delta B^2(k) \rangle \times \left\{ A_p \gamma_k + \text{Im} \frac{\omega - \Omega_p}{k\alpha_{\parallel p}} F^-(A_p, \Omega_p, Z_p) \right\} \quad (12b)$$

$$\frac{dT_{\perp c}}{dt} = -\frac{e^2}{2m_e c^2} \int_{-\infty}^{\infty} \frac{dk}{k^2} \langle \delta B^2(k) \rangle \times \left\{ (2A_c - 1) \gamma_k + \text{Im} \frac{2i\gamma + \Omega_e}{k\alpha_{\parallel c}} F^+(A_c, \Omega_e, Z_c) \right\} \quad (12c)$$

$$\frac{dT_{\parallel c}}{dt} = \frac{e^2}{m_e c^2} \int_{-\infty}^{\infty} \frac{dk}{k^2} \langle \delta B^2(k) \rangle \times \left\{ A_c \gamma_k + \text{Im} \frac{\omega + \Omega_e}{k\alpha_{\parallel c}} F^+(A_c, \Omega_e, Z_c) \right\} \quad (12d)$$

$$\frac{dT_{\perp h}}{dt} = -\frac{e^2}{2m_e c^2} \int_{-\infty}^{\infty} \frac{dk}{k^2} \langle \delta B^2(k) \rangle \times \left\{ (2A_h - 1) \gamma_k + \text{Im} \frac{2i\gamma + \Omega_e}{k\alpha_{\parallel h}} F^+(A_h, \Omega_e, Z_h) \right\} \quad (12e)$$

$$\frac{dT_{\parallel h}}{dt} = \frac{e^2}{m_e c^2} \int_{-\infty}^{\infty} \frac{dk}{k^2} \langle \delta B^2(k) \rangle \times \left\{ A_h \gamma_k + \text{Im} \frac{\omega + \Omega_h}{k\alpha_{\parallel h}} F^+(A_h, \Omega_e, Z_h) \right\} \quad (12f)$$

with

$$F^\pm(A_a, \Omega_a, Z_a) = [A_a \omega \pm \Omega_a (A_a - 1)] Z_a \left( \frac{\omega \pm \Omega_a}{k\alpha_{\parallel a}} \right).$$

In terms of the normalized quantities these equations can be rewritten, respectively, as

$$\frac{d\beta_{\perp p}}{d\tau} = - \int \frac{d\tilde{k}}{\tilde{k}^2} W(\tilde{k}) \left\{ (2A_p - 1) \tilde{\gamma} + \text{Im} \frac{2i\tilde{\gamma} - 1}{\tilde{k}\sqrt{\beta_{\parallel p}}} \times [A_p \tilde{\omega} - (A_a - 1)] Z_p \left( \frac{\tilde{\omega} - 1}{\tilde{k}\sqrt{\beta_{\parallel p}}} \right) \right\} \quad (13a)$$

$$\frac{d\beta_{\parallel p}}{d\tau} = 2 \int \frac{d\tilde{k}}{\tilde{k}^2} W(\tilde{k}) \left\{ A_p \tilde{\gamma} + \text{Im} \frac{\tilde{\omega} - 1}{\tilde{k}\sqrt{\beta_{\parallel p}}} \times [A_p \tilde{\omega} - (A_a - 1)] Z_p \left( \frac{\tilde{\omega} - 1}{\tilde{k}\sqrt{\beta_{\parallel p}}} \right) \right\} \quad (13b)$$

$$\frac{d\beta_{\perp c}}{d\tau} = -\eta_c \int \frac{d\tilde{k}}{\tilde{k}^2} W(\tilde{k}) \left\{ \mu (2A_c - 1) \tilde{\gamma} + \text{Im} \frac{2i\tilde{\gamma} + \mu}{\tilde{k}\sqrt{\beta_{\parallel c}/\eta_c}} \times \tilde{F}(A_c, Z_c, \beta_c, \eta_c) \right\} \quad (13c)$$

$$\frac{d\beta_{\parallel c}}{d\tau} = 2 \eta_c \int \frac{d\tilde{k}}{\tilde{k}^2} W(\tilde{k}) \left\{ \mu A_c \tilde{\gamma} + \text{Im} \frac{\tilde{\omega} + \mu}{\tilde{k}\sqrt{\beta_{\parallel c}/\eta_c}} \times \tilde{F}(A_c, Z_c, \beta_c, \eta_c) \right\} \quad (13d)$$

$$\frac{d\beta_{\perp h}}{d\tau} = -\eta_h \int \frac{d\tilde{k}}{\tilde{k}^2} W(\tilde{k}) \left\{ \mu (2A_h - 1) \tilde{\gamma} + \text{Im} \frac{2i\tilde{\gamma} + \mu}{\tilde{k}\sqrt{\beta_{\parallel h}/\eta_h}} \times \tilde{F}(A_h, Z_h, \chi_h, \beta_h, \eta_h) \right\} \quad (13e)$$

$$\frac{d\beta_{\parallel h}}{d\tau} = 2 \eta_h \int \frac{d\tilde{k}}{\tilde{k}^2} W(\tilde{k}) \left\{ \mu A_h \tilde{\gamma} + \text{Im} \frac{\tilde{\omega} + \mu}{\tilde{k}\sqrt{\beta_{\parallel h}/\eta_h}} \times \tilde{F}(A_h, Z_h, \chi_h, \beta_h, \eta_h) \right\} \quad (13f)$$

with

$$\tilde{F}(A_a, Z_a, \chi_a, \beta_a, \eta_a) = \sqrt{\mu} [A_a \tilde{\omega} + (A_a - 1) \mu] \times Z_a \left( \frac{\tilde{\omega} + \mu}{\tilde{k}\sqrt{\mu} \chi_a \beta_{\parallel a}/\eta_a} \right),$$

and

$$\frac{\partial W(\tilde{k})}{\partial \tau} = 2 \tilde{\gamma} W(\tilde{k}). \quad (14)$$

where  $W(\tilde{k}) = \delta B^2(\tilde{k})/B_0^2$  is the wave energy density,  $\tau = \Omega_p t$ , and  $\chi_c = 1$ .

For the normalization, we keep distinction between the plasma frequencies of the core (subscript  $c$ ) and halo (subscript  $h$ ) electrons, i.e.,  $\omega_{p,a} = \sqrt{4\pi n_a e^2/m_e}$  is defined in terms of the number density  $n_a$ , which is expected to play an important role mainly triggering the effects of these components on instabilities. Normalization to a total plasma frequency  $\omega_{p,e} = \sqrt{4\pi n_0 e^2/m_e}$ , where the total number density  $n_0 = n_c + n_h$ , invoked

in similar studies, e.g., Sarfraz (2018, and refs. therein), may introduce an artificial coupling between the core and halo electrons, and therefore alter their quasilinear relaxation under the effect of firehose fluctuations.

### 3. NUMERICAL RESULTS

This section presents the results of our numerical linear and quasilinear analyses of EFH modes for two distinct sets of plasma parameters, which we name case 1 and case 2. These two cases have chosen to correspond to high and low values of the power-index, e.g.  $\kappa = 8$  in case 1, and  $\kappa = 3$  in case 2, see parametrizations (15) and (16) below. As already motivated in Section 2, this parametrization is suggested by the in-situ measurements of the solar wind electrons in a large interval (0.3 – 3.95 AU) of heliocentric distances (Maksimovic et al. 2005; Štverák et al. 2008; Pierrard et al. 2016; Lazar et al. 2017a).

- Case 1.

$$\begin{aligned} \kappa &= 8, \quad \eta_h = 0.056, \quad W(k) = 10^{-6} \\ A_{c,h}(0) &= \frac{T_{\perp,c,h}(0)}{T_{\parallel,c,h}(0)} = \frac{\beta_{\perp,c,h}(0)}{\beta_{\parallel,c,h}(0)} = 0.1, \\ \beta_c(0) &= 5, 7, 10, \text{ and } \beta_h(0) = \beta_c(0)/3.809, \\ A_p(0) &= 1.0, \quad \beta_p(0) = \beta_c(0)/3. \end{aligned} \quad (15)$$

- Case 2.

$$\begin{aligned} \kappa &= 3, \quad \eta_h = 0.037, \quad W(k) = 10^{-6} \\ A_{c,h}(0) &= \frac{T_{\perp,c,h}(0)}{T_{\parallel,c,h}(0)} = \frac{\beta_{\perp,c,h}(0)}{\beta_{\parallel,c,h}(0)} = 0.1, 0.2, 0.3, \\ \beta_c(0) &= 5, \quad \beta_h(0) = \beta_c(0)/2.236, \\ A_p(0) &= 1.0, \quad \beta_p(0) = \beta_c(0)/3. \end{aligned} \quad (16)$$

#### 3.1. Linear analysis

For a linear analysis we use the dispersion relation (7). Figure 2 and 3 illustrate unstable EFH solutions for case 1 and case 2, respectively. Case 1 ( $\kappa = 8$ ,  $A_{c,h} = 0.1$ ), allows us to compare growth rates for different core plasma betas  $\beta_{\parallel,c} = 5, 7, 10$  (implying different halo plasma betas, respectively,  $\beta_{\parallel,h} = 1.312, 1.84, 2.63$ ). Increasing the plasma beta may slightly enhance the the maximum growth rates (peaks), but markedly diminishes the range of unstable wavenumbers. These counter-balancing effects are also observed for case 2 (not shown here).

In Figure 3 we study the effect of the electron anisotropies  $A_{c,h}(0) = 0.1, 0.2, 0.3$  considering the plasma parameters in case 2 ( $\kappa = 3$ ), as for case 1 the observed variations are similar. The maximum (peaking) growth rates increase as the electron anisotropy

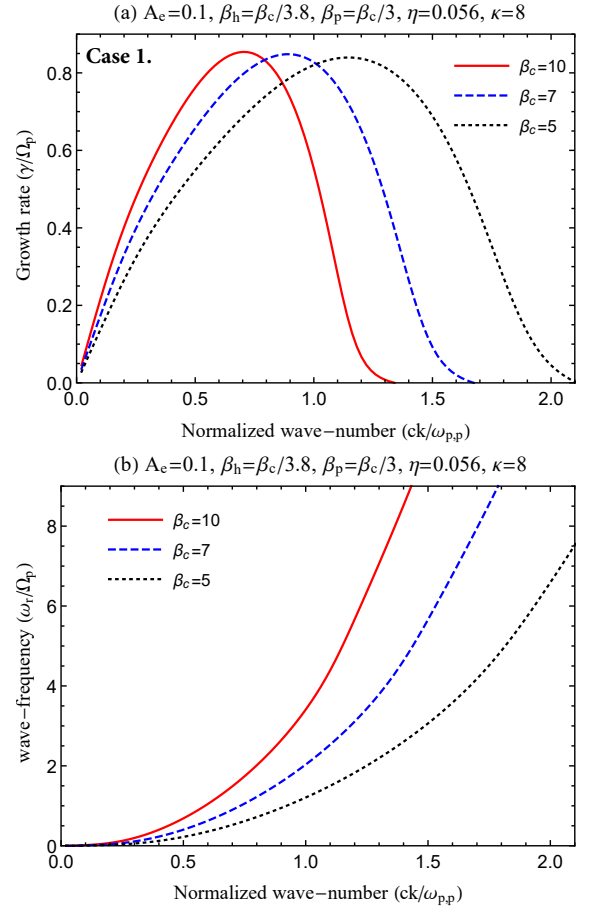


**Figure 2.** Variation of growth rates (top) and wave-frequencies (bottom) with plasma beta.

increases, but the range of unstable wave-numbers decreases. The EFH instability becomes more operative at lower wave numbers by increasing the plasma beta parameters and/or electron anisotropies. The corresponding wave frequencies are increasing with increasing plasma betas and/or the electron anisotropy, see panels (b) in Figures 2 and 3.

We can already highlight the importance of these results and motivate the present study by a comparative analysis between theoretical predictions from linear theory and the observations in the solar wind. We use the same set of slow wind ( $V_{sw} \leq 500 \text{ km s}^{-1}$ ) data mentioned in Section 2, to compare the observed anisotropies with theoretical thresholds of the instability, see Figure 4. Data are displayed in Figure 4 using a histogram plot counting for the number of events with color logarithmic scale. Thresholds of EFH unstable solutions are derived for a maximum growth rate  $\gamma_m = 10^{-3}\Omega_p$  and are fitted to an inverse power-law (Lazar et al. 2018a)

$$A_a = 1 - \frac{s}{\beta_{\parallel,a}^\alpha} \quad (17)$$

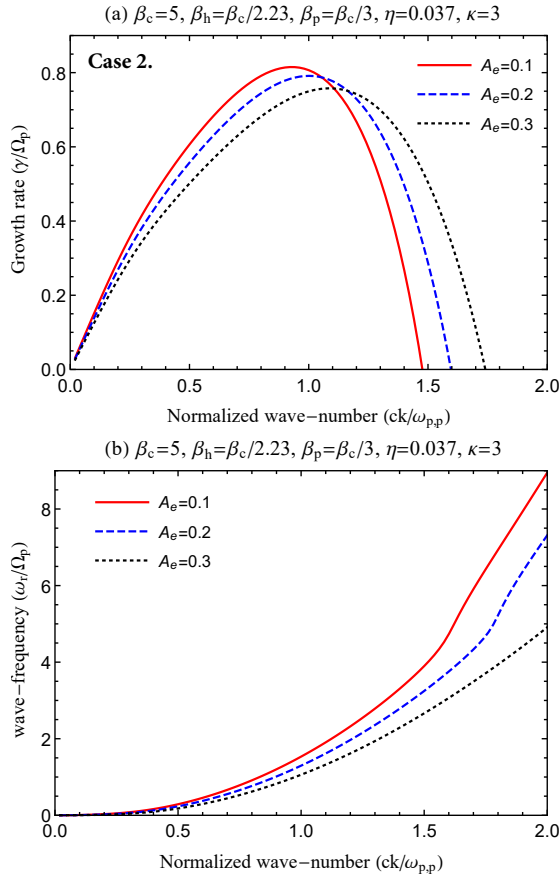


**Figure 3.** Variation of growth rates (top) and wave-frequencies (bottom) with temperature anisotropy.

for the core ( $a = c$ , panel a) and the halo ( $a = h$ , panel b), with fitting parameters  $s$  and  $\alpha$  given in Table 1.

The new instability thresholds from the interplay of the core and halo population (red for  $\kappa = 3$  and blue  $\kappa = 8$ ) are contrasted with those obtained for a single bi-Maxwellian component (dotted black). We should observe that these new thresholds markedly decrease approaching and shaping much better the limits of the halo anisotropy (panel b). The lower threshold is obtained in this case for a higher  $\kappa = 8$  (blue, case 1), under the influence of a more dense halo (comparing to case 2). We can also admit minor (but still visible) changes of the instability thresholds constraining the core anisotropy (panel a). The instability driven by the core populations is stimulated by the anisotropic halo, but lower thresholds are obtained for a more dense core (red, case 2).

### 3.2. Quasilinear analysis

Beyond the linear theory, the quasilinear (QL) analysis describes the temporal evolution of electromagnetic fluctuations, which are enhanced by the instabil-

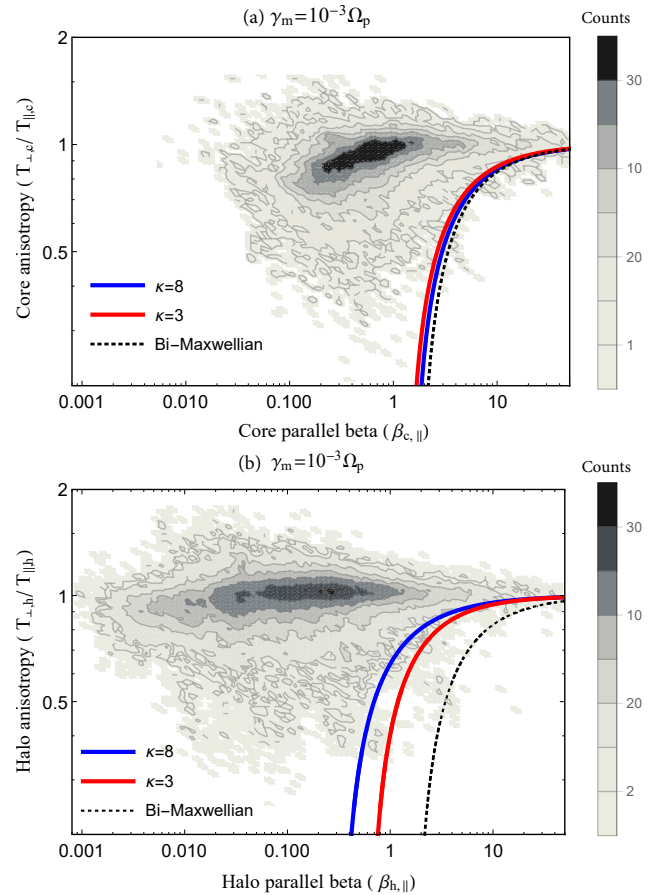


**Figure 4.** A comparison between theoretical anisotropy thresholds and the slow solar wind observational data for the core (panel a), and halo (panel b) anisotropies.

ity and turn to change the main features of the distributions, such as temperature components ( $T_{\perp,\parallel}$ ), the anisotropy ( $A_a = T_{\perp}/T_{\parallel}$ ), and implicitly the plasma betas ( $\beta_{\perp}/\beta_{\parallel} \equiv T_{\perp}/T_{\parallel}$ ). However, we assume no exchange of electrons between core and halo, i.e.  $\eta_h/\eta_c$  is constant, and the shape of the distributions preserves, for instance, the protons and electron core remain Maxwellian, while the electron halo remain Kappa-distributed with the same value of power-index. The recent comparisons of the QL theory with the particle-in-cell simulation by Yoon et al. (2017a) and Lazar et al. (2018b), show a reasonable agreement for the temporal evolution of the electron VDFs. There are also some indications from Vlasov simulations that power-index does not change much in the QL relaxation, though these results are still limited to studies of different instabilities (Lazar et al. 2017c). We resolve the system of QL equations (13) and (14) for the same plasma parameters introduced here above as cases 1 and 2.

Figure 5 describes the time evolution of the perpendicular (red) and parallel (blue) plasma betas for the

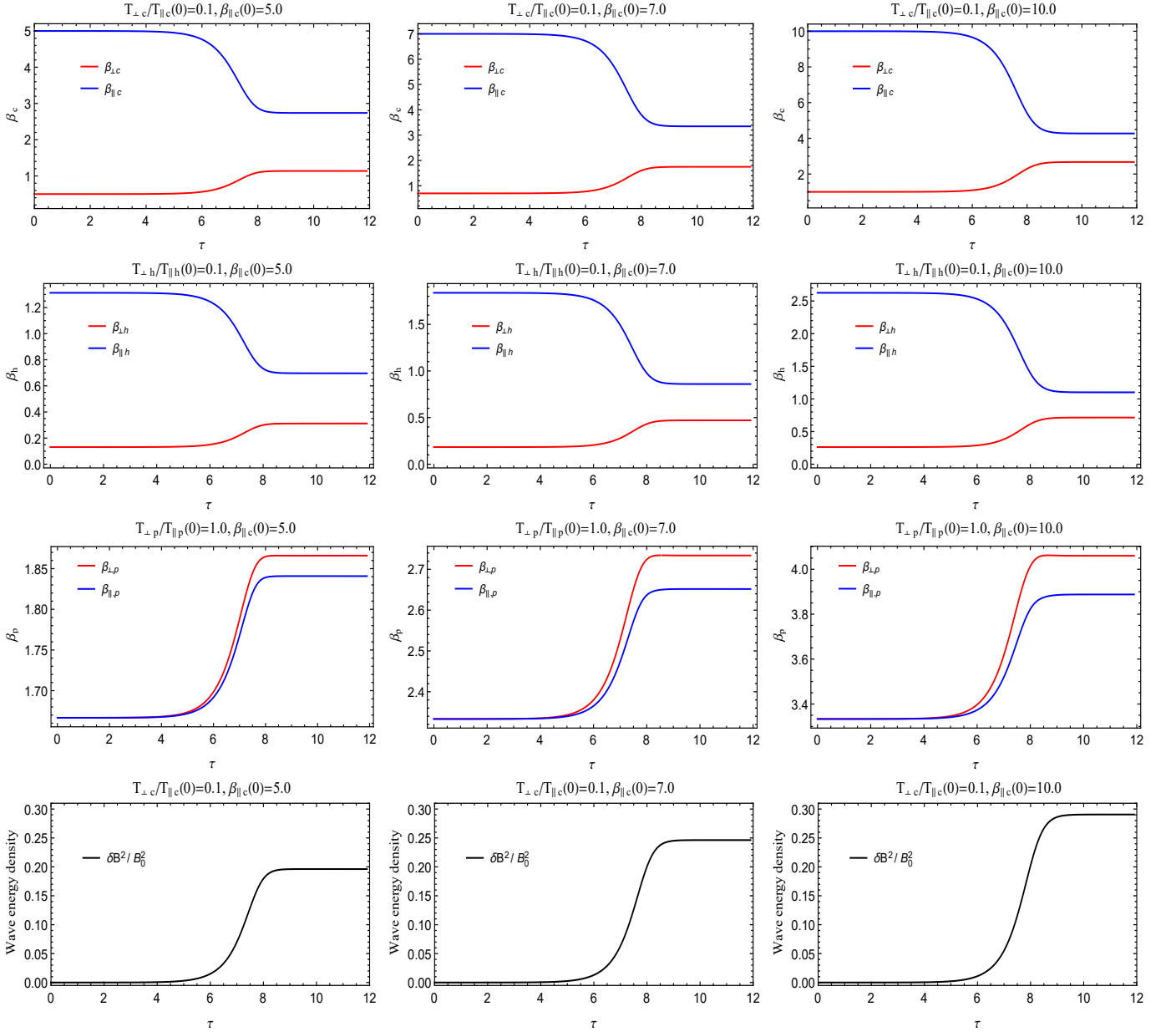


**Figure 5.** Case 1: Time evolution of the normalized parallel and perpendicular plasma betas for the core electrons (top panels), halo electrons (middle-first), protons (middle-second), and the wave energy density (bottom panels) for different initial conditions:  $\beta_{c,\parallel}(0) = 5.0, 7.0, 10.0$ .

electron components, core (top) and halo (middle-first), thermal protons (middle-second), and the corresponding variation of the wave energy density  $\delta B^2/B_0^2$  (bottom) as functions of the normalized time  $\tau = \Omega_p t$  for case 1 ( $\kappa = 8$ ) and different initial plasma betas  $\beta_c(0) = 5.0$  (left),  $7.0$  (middle), and  $10.0$  (right). The excitation of the EFH instability from the interplay of the anisotropic core and halo can regulate the initial temperature anisotropy for both these two components and also for protons, through the cooling and heating mechanisms reflected by the parallel (blue) and perpendicular

(red) plasma betas. The level of saturated fluctuations is increasing with increasing the initial plasma beta, i.e.  $\beta_c(0) = 10.0$ , confirming a stimulation of the instability predicted for the peaking growth rates by the linear theory in Figure 2(a). Nevertheless, both the core and halo components show similar intervals of relaxation, but the halo remains slightly less anisotropic than the core after the instability saturation, i.e.,  $\tau_m = 12$ . Linear theory cannot describe quantitatively the energy transfer between plasma particles mediated by the instability. However, from a quasilinear analysis we can estimate

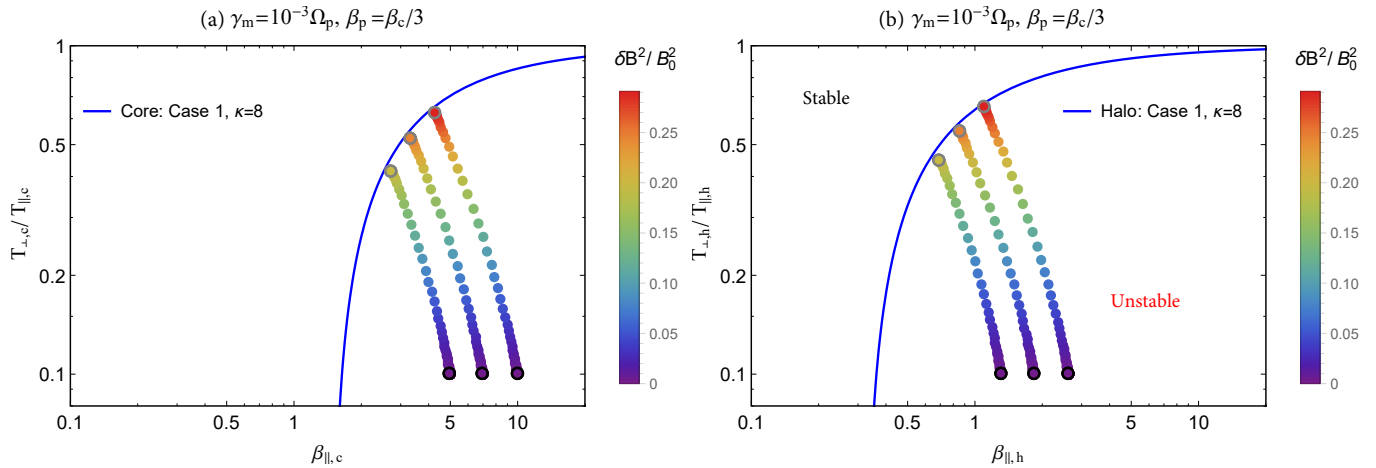


**Figure 6.** Case 1: Dynamical paths for the core (panel a) and halo (panel b) anisotropies showing the level of magnetic field fluctuations with color levels. Initial states are indicated by black circles, while the final positions are marked with gray circles.

these exchanges induced by the free energy of electrons, which is transferred during the instability growing to the protons: Third row of panels shows the time evolution of the parallel and perpendicular plasma betas for protons ( $\beta_{\perp,\parallel,p}$ ), which are initially isotropic, i.e.,  $A_p(0) = 1$ . Both beta components are increased as  $\tau$  increases, but protons are heated more in perpendicular direction and become anisotropic at later stages  $A_p(\tau_m) > 1.0$ . Their anisotropy increases with increasing the initial plasma beta. These evolutions confirm, see (Paesold & Benz 1999; Messmer 2002; Paesold & Benz 2003), that a finite amount of free energy is transferred by the growing fluctuations to the protons, especially in direction perpendicular to the background magnetic field.

Figure 6 presents temporal profiles of the temperature anisotropy and parallel plasma betas in a  $(A_a, \beta_{\parallel,a})$ -space, for both the core (subscript “ $a = c$ ”, in panel a) and halo (subscript “ $a = h$ ”, in panel b). Black circles indicate the initial positions, while the gray circles mark the limit states after saturation. The associated wave energy density  $\delta B^2/B_0^2$  is coded with colors. As expected, final states align along the anisotropy thresholds predicted by the linear theory, with unstable regimes located below the thresholds. This time evolutions clearly shows deviations from isotropy decrease towards less unstable regimes closer marginal stability. These relaxations of the core and halo anisotropies are a direct consequence of the EFH instability and the enhanced electromagnetic fluctuations, which scatter the particles towards quasi-stationary states. This is confirmed by the increase of the wave energy density as the electrons become less anisotropic.

The results in Figure 7 are obtained for case 2 ( $\kappa = 3$ ), with an initial  $\beta_c(0) = 5.0$  and different anisotropies  $A_c(0) = A_h(0) = 0.3$  (left), 0.2 (middle), 0.1 (right).

The main effects, associated with the heating or cooling of different particle populations by the enhanced fluctuations, are reflected by the temporal profiles of the beta components for core, halo, and protons. These effects are similar to those in case 1, but here are mainly triggered by the different anisotropies, e.g., for higher anisotropies, i.e.  $A_{c,h}(0) = 0.1$  (right column), the resulting magnetic wave energy  $\delta B^2/B_0^2$  increases as an effect of the enhancement of the instability growth rates predicted by the linear theory in Figure 3 (a). This may also explain the increase of the energy transferred to the initially isotropic protons ( $A_p(0) = 1.0$ ), which reach moderate anisotropies  $A_p(\tau_m) > 1.0$  after saturation.

In Figure 8 we display dynamical paths of the temperature anisotropy and the parallel plasma beta in a  $(A_a, \beta_{\parallel,a})$ -space for both the core (panel a) and halo (panel b). The initial anisotropies  $A_a(0)$  are marked with black circles, while anisotropies  $A_a(\tau_m)$  at final stages are indicated by gray circles. The levels of the magnetic wave energy  $\delta B^2/B_0^2$  are coded with colors. As in case 1 (Figure 6), the initial deviations from isotropy are reduced in time, towards less unstable states. It is obvious that final states tend to align to the instability thresholds, and larger initial anisotropies, e.g.,  $A_a(0) = 0.1$ , will determine longer dynamical path for the particles. Nevertheless, in Figure 8 the final states of electron anisotropies reach a more stable regime by comparison to Figure 6. One plausible explanation for this physical behavior can be found in the increase of the suprathermal population which stimulate the energy exchange during the instability development to protons, enhancing their anisotropy ( $T_{\perp} > T_{\parallel}$ ), while the core and halo electrons become less anisotropic. This explanation is also supported by the results in Figure 5, left panels, and Figure 7, right panels, which are obtained



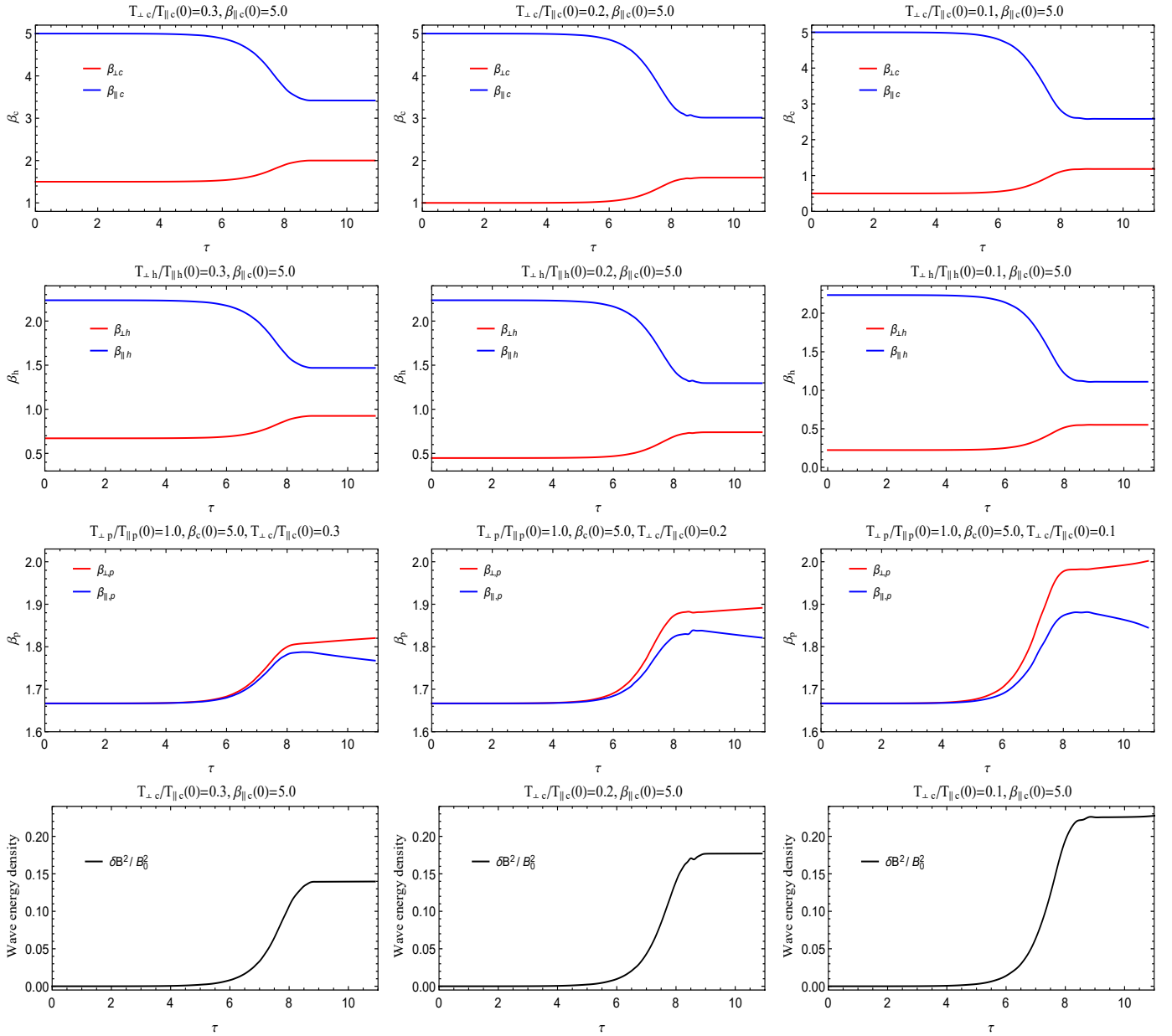


**Figure 7.** Case 2: Time evolution of the normalized parallel and perpendicular plasma betas for the core electrons (top), halo electrons (middle-first), protons (middle-second), and the wave energy density (bottom) for different initial conditions given explicitly in the panels.

for  $\beta_c(0) = 5.0$  and  $A_e(0) = 0.1$ , but different values of the power-index  $\kappa = 8$  (Figure 5) and 3 (Figure 7). It is obvious that at later stages both the proton anisotropy and the associated magnetic wave energy obtained for  $\kappa = 3$ . i.e.  $\delta B^2/B_0^2 = 0.24$  and  $A_p(\tau_m) = 1.08$ , are higher than those obtained for  $\kappa = 8$ , i.e.  $\delta B^2/B_0^2 = 0.2$  and  $A_p(\tau_m) = 1.016$ .

In both these two cases the initial proton plasma beta  $\beta_{\parallel p}(0) = \beta_{\parallel c}(0)/3 > 1.0$  is relatively large, and transfer of energy from electrons to protons remains modest. Dynamical paths of the proton anisotropy are very short in these cases, and we have not displayed them in

Figures 6 and 8. Seeking completeness, we extend the analysis for a series of new cases in Figures 9 and 10, which allow us to examine the mutual effects between the electron populations and protons with relatively low initial  $\beta_{\parallel p}(0) = 0.05$ .

Figure 9 presents by comparison temporal profiles of temperature anisotropy for the core (top) and halo (middle), as well as the associated magnetic wave energy (bottom) for the same plasma parameters in case 1, but for two different initial proton plasma betas, either large  $\beta_{\parallel p}(0) = \beta_{\parallel c}(0)/3 > 1.0$  (dotted lines), or small  $\beta_{\parallel p}(0) = 0.05$  (solid lines). It is clear that protons with

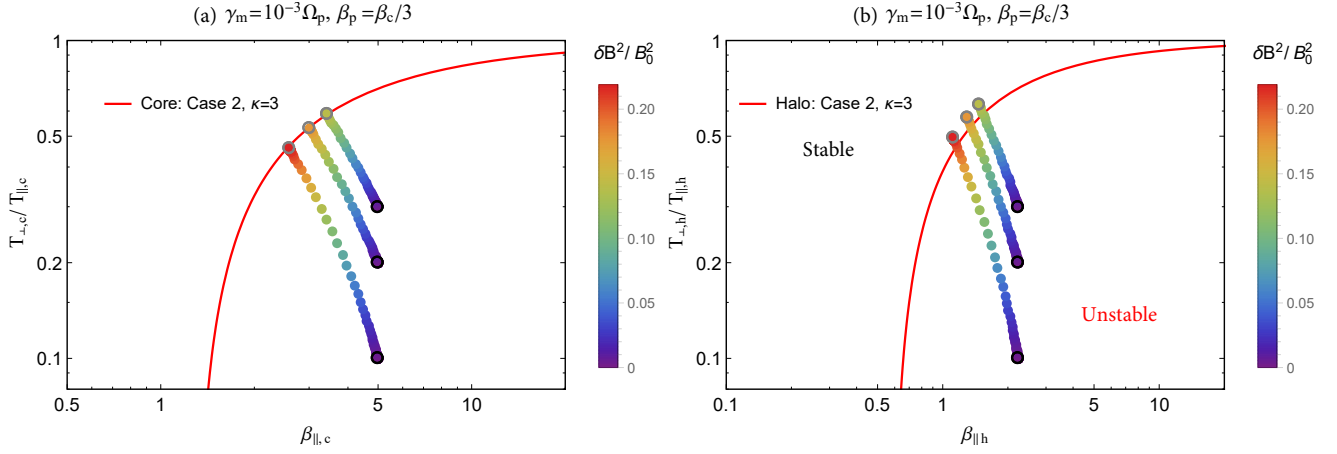


**Figure 8.** The same as in Figure.6 but for Case 2.

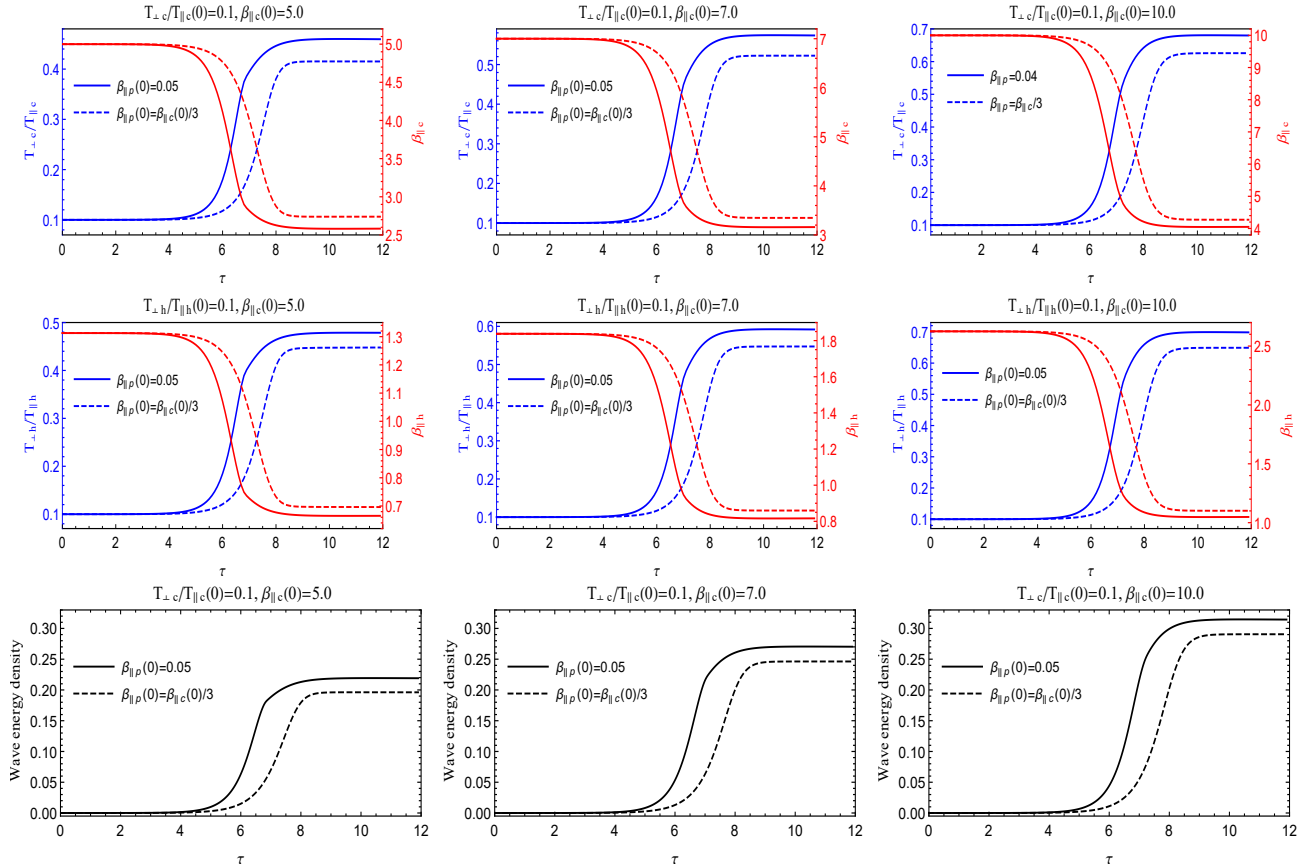


**Figure 9.** Comparison between the effects of protons in Case 1 with  $\beta_{\parallel p}(0) = \beta_{\parallel c}(0)/3$  (dashed lines) and protons with relatively low plasma beta  $\beta_{\parallel p}(0) = 0.05$  (solid lines).

lower beta stimulate the cooling process of both populations of electrons, making it faster, and the core and halo electrons become less anisotropic in this case (solid blue lines). The associated wave energy is enhanced with decreasing proton parallel beta, confirming the enhanced relaxation of the anisotropies. The dynamical

paths of the core, halo and proton anisotropies for the new case with lower  $\beta_{\parallel p}(0) = 0.05$  are displayed in Figure 10. For the core and halo the paths are orientated in the direction of stable regimes and end up or close to the anisotropy thresholds (blue lines) predicted by the linear theory in Figure 4. This behavior suggests

that for low plasma betas  $\beta_{\parallel,p} = 0.05$ , the free energy of electrons is transferred via the growing fluctuations to the (resonant) protons, and especially in perpendicular direction. Thus, at later stages after saturation both core and halo become less anisotropic, while the initially isotropic protons become strongly anisotropic  $A_p(\tau_m) > 1$ , which is evident in Figure 10. These variations are stimulated by increasing the initial plasma beta, i.e.  $\beta_{\parallel,c}(0) = 10.0$ . Protons with temperature anisotropy  $A_p > 1$  may trigger LH polarized electromagnetic ion cyclotron (EMIC) instability with a maximum growth rate in the parallel direction to the background magnetic field (Shaaban et al. 2015, 2016). Shaaban et al. (2017) show that an anisotropic electrons with  $A_e < 1.0$  and their suprathermal populations may stimulate the EMIC unstable modes. These predictions from linear theory seems to be confirmed and explained by the present quasilinear analysis. For a visual guidance Figure 10 displays also the EMIC anisotropy threshold (black line) derived by Shaaban et al. (2017), with fitting parameters  $s = -1.221$  and  $\alpha = 0.579$  in Eq.(17). For  $\beta_{\parallel,c}(0) = 0.05$ , protons (with  $A_p(0) = 1$ ) gain anisotropy in perpendicular direction and move towards the EMIC thresholds, and then their anisotropy decreases to settle down much below the instability threshold after saturation.

From a comparison of our results in Figure 10 with those in a recent study by Sarfraz (2018, Figure 4 therein), we find a reasonable agreements for the dynamical paths of the proton anisotropies, but not for the instability thresholds and paths predicted for the core and halo electrons by the linear and quasilinear approaches. Contrary to Sarfraz (2018) the halo anisotropy threshold is lower than that obtained for the core anisotropy threshold, and extends to lower parallel plasma beta. Our results, from both linear and the quasilinear analyses, show an excellent agreement with the observational limits of the core and halo anisotropies, and this mainly explains by the more realistic plasma parametrization used in our analysis.

#### 4. CONCLUSIONS

In-situ measurements of the velocity distributions of solar wind electrons reveal two central components, a bi-Maxwellian thermal core and a bi-Kappa suprathermal halo (Štverák et al. 2008). Recently Pierrard et al. (2016) have also shown that the core and halo electrons are not independent of each other, and their properties may show direct correlations. These correlations allow us to characterize the instability in terms of either the core or halo parameters. Of particular interest are the highest growing modes which arise when both the core

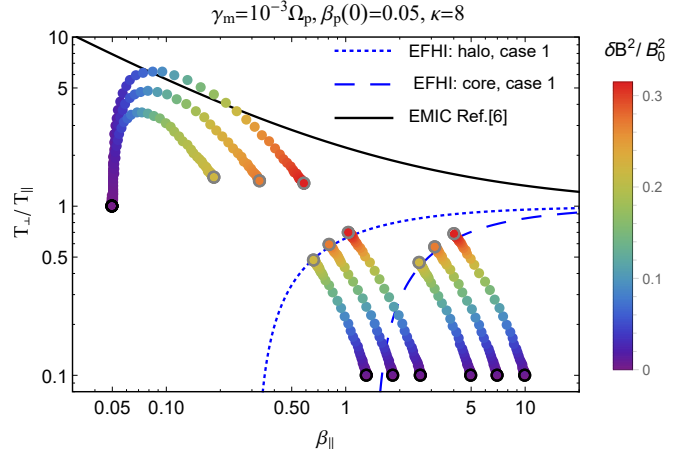


Figure 10. Dynamical paths of case 1, but with  $\beta_{\parallel,p} = 0.05$ .

and halo electrons exhibit similar anisotropies, in our case  $A_{a=h,c} = T_{a,\perp}/T_{a,\parallel} < 1$ . The firehose instability conditions are significantly changed by the interplay of these two populations, such that the thresholds of the periodic branch approach very well the limits of temperature anisotropy reported by the observations for both the core and halo electrons.

We have performed a numerical analysis for both linear dispersion and quasilinear equations derived in Section 3, for conditions typically encountered in the slow wind. Mutual effects of the core and suprathermal halo can markedly stimulate the instability and induce new unstable regimes instability, lowering the instability thresholds by comparison to those provided by the idealized theories of Maxwellian distributed plasmas. The same effects are reflected by the quasilinear saturation of the instability and the relaxation of temperature anisotropy towards the anisotropy thresholds. The evolution of both the core and halo electrons is characterized by perpendicular heating and parallel cooling, lowering their anisotropies during the development of the firehose instability. The relaxation of the temperature anisotropy is found to be associated with an enhancement of the magnetic wave power before reaching the saturation. Protons gain energy from the left-handed electromagnetic fluctuations, especially in direction transverse to the magnetic field, and this energy transfer becomes more important for protons with a low initial plasma beta (i.e.,  $\beta_p(0) = 0.05$ ).

In this study, we have restricted ourselves to the unstable periodic firehose modes that develop with a highest growth rate in directions parallel to the background magnetic field. A QL approach of the aperiodic firehose modes growing faster in the oblique directions (Li & Habbal 2000; Gary & Nishimura 2003; Shaaban et al. 2019) is not yet feasible, but our present results will cer-

tainly stimulate an extended analysis. Furthermore, the influence of the solar wind inhomogeneity (e.g., Yoon (2016); Yoon & Sarfraz (2017b)) has not been considered in the present analysis, and their interplay with the effects of suprathermal electrons will be investigated in the future.

**Table 1.** Fitting parameters for thresholds  $\gamma_m/\Omega_p = 10^{-2}$

| $\kappa$ | Core |          | Halo |          | SBM  |          |
|----------|------|----------|------|----------|------|----------|
|          | $s$  | $\alpha$ | $s$  | $\alpha$ | $s$  | $\alpha$ |
| 3        | 1.32 | 0.994    | 0.6  | 1.03     | –    | –        |
| 8        | 1.45 | 1.0      | 0.35 | 0.88     | –    | –        |
| $\infty$ | –    | –        | –    | –        | 1.75 | 1.04     |

The authors acknowledge support from the Katholieke Universiteit Leuven, Ruhr-University Bochum, and

Alexander von Humboldt Foundation. These results were obtained in the framework of the projects SCHL 201/35-1 (DFG-German Research Foundation), GOA/2015-014 (KU Leuven), G0A2316N (FWO-Vlaanderen), and C 90347 (ESA Prodex 9). S.M. Shaaban would like to acknowledge the support by a Postdoctoral Fellowship (Grant No. 12Z6218N) of the Research Foundation Flanders (FWO-Belgium). P.H.Y. acknowledges the BK21 Plus grant (from NRF, Korea) to Kyung Hee University, and financial support from GFT Charity Inc., to the University of Maryland. Thanks are due to Š. Štverák for providing the observational data.

## REFERENCES

- Chew, G. F., Goldberger, M. L., & Low, F. E. 1956, Proc. Math. Phys. Eng. Sci., 236, 112.  
<http://doi.org/10.1098/rspa.1956.0116>
- Fried, B., & Conte, S. 1961, The Plasma Dispersion Function (Academic Press).  
<https://doi.org/10.1016/B978-1-4832-2929-4.50005-8>
- Ganse, U., Kilian, P., Vainio, R., & Spanier, F. 2012, SoPh, 280, 551. <http://doi.org/10.1007/s11207-012-0077-7>
- Gary, S. P., Jian, L. K., Broiles, T. W., et al. 2016, J. Geophys. Res., 121, 30.  
<http://doi.org/10.1002/2015JA021935>
- Gary, S. P., & Nishimura, K. 2003, Physics of Plasmas, 10, 3571. <http://doi.org/10.1063/1.1590982>
- Gershman, D. J., F-Vinãs, A., Dorelli, J. C., et al. 2017, Nat. Commun., 8, 1.  
<http://doi.org/10.1038/ncomms14719>
- Hellinger, P., Trávníček, P., Kasper, J. C., & Lazarus, A. J. 2006, Geophys. Res. Lett., 33, 2.  
<http://doi.org/10.1029/2006GL025925>
- Jian, L., Wei, H., Russell, C., et al. 2014, ApJ, 786, 123.  
<http://doi.org/10.1088/0004-637X/786/2/123>
- Kasper, J. C., Lazarus, A. J., Steinberg, J. T., Ogilvie, K. W., & Szabo, A. 2006, J. Geophys. Res., 111, 1.  
<http://doi.org/10.1029/2005JA011442>
- Lazar, M., Pierrard, V., Shaaban, S., Fichtner, H., & Poedts, S. 2017a, A&A, 602, A44.  
<https://doi.org/10.1051/0004-6361/201630194>
- Lazar, M., & Poedts, S. 2009, A&A, 494, 311.  
<https://doi.org/10.1051/0004-6361:200811109>
- Lazar, M., Poedts, S., & Fichtner, H. 2015, A&A, 582, A124. <https://doi.org/10.1051/0004-6361/201526509>
- Lazar, M., Schlickeiser, R., & Shukla, P. K. 2008, Phys. Plasmas, 15, 042103. <https://doi.org/10.1063/1.2896232>
- Lazar, M., Shaaban, S., Poedts, S., & Štverák, Š. 2017b, MNRAS, 464, 564.  
<https://doi.org/10.1093/mnras/stw2336>
- Lazar, M., Shaaban, S. M., Fichtner, H., & Poedts, S. 2018a, Phys. Plasmas, 25, 022902.  
<https://doi.org/10.1063/1.5016261>
- Lazar, M., Yoon, P., & Eliasson, B. 2017c, Phys. Plasmas, 24, 042110. <https://doi.org/10.1063/1.4979903>
- Lazar, M., Yoon, P. H., López, R. A., & Moya, P. S. 2018b, J. Geophys. Res., 123, 6.  
<http://doi.org/10.1002/2017JA024759>
- Li, X., & Habbal, S. R. 2000, J. Geophys. Res., 105, 27377.  
<http://doi.org/10.1029/2000JA000063>
- Maksimovic, M., Zouganelis, I., Chaufray, J.-Y., et al. 2005, J. Geophys. Res., 110.  
<https://doi.org/10.1029/2005JA011119>
- Messmer, P. 2002, A&A, 382, 301.  
<https://doi.org/10.1051/0004-6361:20011583>
- Paesold, G., & Benz, A. O. 1999, A&A, 351, 741.  
<http://adsabs.harvard.edu/full/1999A%26A...351..741P>
- . 2003, A&A, 401, 711.  
<https://doi.org/10.1051/0004-6361:20030113>
- Pierrard, V., & Lazar, M. 2010, SoPh, 267, 153.  
<https://doi.org/10.1007/s11207-010-9640-2>

- Pierrard, V., Lazar, M., Poedts, S., et al. 2016, *SoPh*, 291, 2165. <https://doi.org/10.1007/s11207-016-0961-7>
- Sarfraz, M. 2018, *J. Geophys. Res.*, 123, 6107. <https://doi.org/10.1029/2018JA025449>
- Sarfraz, M., Saeed, S., Yoon, P. H., Abbas, G., & Shah, H. A. 2016, *J. Geophys. Res.*, 121, 9356. <http://doi.org/10.1002/2016JA022854>
- Sarfraz, M., Yoon, P., Saeed, S., Abbas, G., & Shah, H. 2017, *Physics of Plasmas*, 24, 012907. <https://doi.org/10.1063/1.4975007>
- Shaaban, S., Lazar, M., Poedts, S., & Elhanbaly, A. 2016, *J. Geophys. Res.*, 121, 6031. <https://doi.org/10.1002/2016JA022587>
- Shaaban, S. M., Lazar, M., López, R. A., Fichtner, H., & Poedts, S. 2019, *Monthly Notices of the Royal Astronomical Society*, 483, 5642. <https://doi.org/10.1093/mnras/sty3377>
- Shaaban, S. M., Lazar, M., Poedts, S., & Elhanbaly, A. 2015, *ApJ*, 814, 34. <https://doi.org/10.1088/0004-637X/814/1/34>
- . 2017, *Ap&SS*, 362, 13. <https://doi.org/10.1007/s10509-016-2994-7>
- Štverák, Š., Trávníček, P., Maksimovic, M., et al. 2008, *J. Geophys. Res.*, 113, A03103. <https://doi.org/10.1029/2007JA012733>
- Vasyliunas, V. M. 1968, *J. Geophys. Res.*, 73, 2839. <https://doi.org/10.1029/JA073i009p02839>
- Vinãs, A. F., Gaelzer, R., Moya, P., Mace, R., & Araneda, J. 2017, in *Kappa Distributions*, ed. G. Livadiotis (Elsevier), 329 – 361. <https://doi.org/10.1016/B978-0-12-804638-8.00007-3>
- Yoon, P. H. 2016, *ApJ*, 833, 106. <https://doi.org/10.3847/1538-4357/833/1/106>
- Yoon, P. H., López, R. A., Seough, J., & Sarfraz, M. 2017a, *Physics of Plasmas*, 24, doi:10.1063/1.4997666. <http://doi.org/10.1063/1.4997666>
- Yoon, P. H., & Sarfraz, M. 2017b, *ApJ*, 835, 1. <https://doi.org/10.3847/1538-4357/835/2/246>
- Yoon, P. H., Seough, J. J., Kim, K. H., & Lee, D. H. 2012, *Journal of Plasma Physics*, 78, 47. <http://doi.org/10.1017/S0022377811000407>